Sensing and Bio-Sensing Research 47 (2025) 100727

Contents lists available at ScienceDirect

Sensing and Bio-Sensing Research

journal homepage: www.elsevier.com/locate/sbsr

Smart sensing of creatinine in urine samples: Leveraging Cu-nanowires/ MoS_2 quantum dots and machine learning

Geethukrishnan [a], Paresh Prakash Bagde [b], Sammishra KH [c], Chandranath Adak [b], Rajendra P. Shukla [d], Kiran Kumar Tadi [a,*]

[a] *Energy, Electrodics and Electrocatalysis (EEE) Research Lab, Department of Chemistry, School of Advanced Sciences, Vellore Institute of Technology, Chennai 600127, India*
[b] *Department of Computer Science and Engineering, Indian Institute of Technology Patna, Bihar 801106, India*
[c] *Department of Computer Science, SDM College (Autonomous), Ujire, D.K 574240, Karnataka, India*
[d] *Department of Electrical and Computer Engineering, North Carolina State University, Raleigh, NC 27695, USA*

ARTICLE INFO

Keywords:
Electrochemical sensor
Copper nanowires
Artificial neural networks
Machine learning
Creatinine

ABSTRACT

Serum creatinine (CRT) levels are key biomarkers for diagnosing, staging, and monitoring renal disease in clinical practice. In this work, copper nanowires (CuNW), and Molybdenum disulfide quantum dots (MSQD) modified glassy carbon electrode (GCE) were chosen to demonstrate the electrochemical detection of CRT in complex mixture and urine samples. The materials were characterized using various physical characterizations such as FESEM, XRD, UV, PL, and FT-Raman. The electrocatalytic activity of the sensor was investigated using cyclic voltammetry (CV), and differential pulse voltammetry (DPVs). Despite the elevated sensitivity and cost-effectiveness of electrochemical sensors, the performance of the sensors is constrained by the existence of interfering species that generate conflicting and overlapping electrochemical signatures. In order to address this issue, we implemented a machine learning (ML) approach to accurately quantify CRT levels in complex mixtures, as well as in urine samples. The ML algorithms employed are trained and tested on a large dataset, allowing them to effectively capture and analyze the variance in the electrochemical signatures, demonstrating the application of artificial intelligence. The proposed sensor exhibits linearity from 1.96 μM to 966.0 μM and shows the best performance in terms of limit-of-detection (LOD) of 2.3 μM in a complex mixture and 0.001 μM in real urine samples, with RMSE of 0.2 and 0.017 μM using artificial neural network and random forest ML models respectively. We anticipate that by further miniaturization of these sensors into point-of-care testing devices, renal diseases can be managed effectively.

1. Introduction

Creatinine (2-amino-1-methyl-5H-imidazole-4-one (CRT)) is the final product of creatine metabolism in mammals [1]. So, it becomes an important clinical analyte used to diagnose muscle, thyroid, and renal functions. Clinical practice must assess the amount of CRT in human blood and urine since it reflects the functioning of the thyroid, kidney, and muscles. Muscle tissue uses creatine as its source of energy as a consequence of the breakdown of amino acids. It gets transported through blood as a dehydrogenated substance known as CRT. The glomerular ultrafiltration rate (GFR) and the net amount of CRT in serum are indirectly proportional, showing both the quantitative and qualitative functionality of the kidneys [2]. The normal physiological range for CRT in the blood and urine is 40–150 μM and 5.92–19.01 mM respectively [1,3], but in the case of some pathological conditions, the CRT range will exceed the normal range. Urine CRT is consistently excreted at a stable rate through glomerular filtration. The property facilitates the assessment of renal glomerular filtration rate and standardizing urinary biomarkers [4,5]. Furthermore, detecting CRT in urine is a non-invasive and convenient alternative to the conventional serum CRT measurement. This opens up possibilities for its utilization in home healthcare settings, offering the potential for broader application in monitoring healthcare status. Therefore, it becomes crucially vital from a clinical standpoint to measure the levels of CRT in human urine samples. Patients with acute renal injury who are critically ill may benefit from routine CRT monitoring with quick results availability and

---

[*] Corresponding author.
E-mail address: kirankumar.tadi@vit.ac.in (K.K. Tadi).

https://doi.org/10.1016/j.sbsr.2024.100727
Received 28 October 2024; Received in revised form 16 December 2024; Accepted 19 December 2024

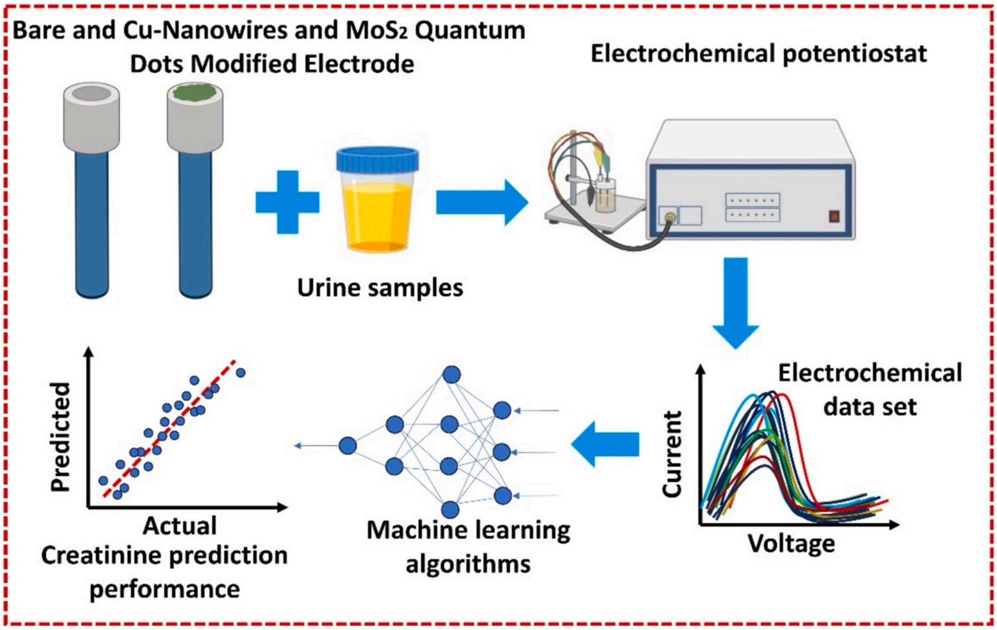

Fig. 1. Schematic illustration of the electrochemical determination of CRT in urine samples.

peritoneal dialysis patients may see an improvement in quality of life [5,6].

The commonly used conventional methods to analyze CRT are based on a colorimetric method using Jaffe's reaction [7] or an enzymatic method using multiple enzymes (mostly electrochemical sensing) [8]. However, a variety of metabolites and drugs present in biological samples could adversely affect colorimetric procedures [9], whereas enzymic assays are time-consuming, difficult, and expensive. Some chromatographic methods can determine CRT in biofluids in a highly selective and relatively quick manner [10] but the instruments required for these methods are expensive, time-consuming to prepare the samples, and skilled personnel to operate. On the other hand, although enzymatic techniques offer excellent selectivity, they tend to be costly and complex. Thus, there is an urgent need for a dependable method to detect CRT that is both affordable and straightforward. Using creatininase, creatinase, and sarcosine oxidase, an enzymatic electrochemical approach was created to increase the specificity of the system [11], and the detection of CRT was accomplished by monitoring an electroactive product (hydrogen peroxide) produced by the series of enzymatic reactions using cyclic voltammetry (CV) or amperometry [12,13]. Due to its multiple component complexity, it results in high cost and complexity in reaction [14]. Therefore, a practical clinical need for creating a simple, affordable, speedy technology for measuring CRT still exists.

Over the last ten years, several novel analysis methods have been utilized to progressively ascertain CRT levels. Recently numerous advanced analytical methods have been applied [15]. These techniques predominantly utilize conventional instrument analysis methods, including colorimetric assays, high-performance liquid chromatography-mass spectrometry/mass spectrometry (HPLC-MS/MS), and capillary electrophoresis, for the qualitative or quantitative assessment of CRT [16]. Instrumental analysis methods frequently necessitate rigorous procedures, intricate pre-treatments, time-intensive protocols, and prolonged analysis durations, resulting in diminished efficiency in CRT detection. Particularly, electrochemical sensors stand out as excellent options for biomolecule detection due to their distinctive and substantial benefits, which encompass straightforward handling, rapid signal responsiveness, compact instrument size, minute sample requirement, affordability, and heightened sensitivity [17].

Electroanalytical techniques play a vital role in the accurate and simple quantification of several bioanlaytes [18,19]. They were thoroughly identified and measured in multiple biological fluids, including serum, urine, and synthetic matrices, wherein their concentration serves as a critical biomarker for the early detection of chronic diseases. Electroanalytical methods, DPV, and EIS (in the case of electro-inactive species) [20,21] are characterized by their remarkable sensitivity, swift response times, and capacity to analyze complex biological matrices with minimal sample preprocessing. These methodologies are especially beneficial in point-of-care settings and for real-time surveillance, facilitating rapid and on-site assessment of ultra-low levels concentration of biomarkers.

One predominant approach for CRT detection involves the application of electrochemical methods, encompassing both enzymatic and non-enzymatic sensor modalities [22]. This has prompted research into a novel class of electrochemical CRT sensors that show high selectivity and sensitivity while having strong stability and not necessitating the use of enzymes. It's important to note that the enzymatic sensor systems exhibit low stability, sensitivity, and reproducibility as the enzymes tend to denature. Enzymatic sensors are expensive and prone to denaturation with prolonged use. The proposition of employing non-enzymatic sensors for CRT detection has arisen as a strategic response to circumvent these challenges. Compared to enzymatic CRT sensors there are fewer studies on non-enzymatic biosensors. In these non-enzymatic sensors, the sensing is often accomplished by CRT interaction with chemically synthesized nanoparticles that are embedded at the electrode surface [23], with a supporting media [24], or as a composite [25]. Additionally, molecularly imprinted polymers (MIPs) can be used to create an artificial lock and key system [26]. Unlike their enzymatic analogs, these non-enzymatic electrochemical sensors provide remarkable storage stability, reproducibility, and flexibility. For instance, sensitive CRT biosensors have been created by using the unique interaction between CRT and metallic centers. These sensors show robust storage stability, minimum signal reduction, and good response for clinical detection. Further research is necessary to comprehend how CRT interacts with the active metallic detecting sites. Due to the ease of fabrication, they lead to pertinent clinical detection with minimum interferences but suffer from a large range of interferents that are found in human biological fluids in terms of both diversity and concentration [27].

Due to their exceptional electrocatalytic activity, good stability, and low cost, transition metals, and metal oxides have been attracting more attention as electrode system modifiers, because they may facilitate electron transfer reactions at low potentials [28,29]. A soluble CRT-metal complex can be generated by the transition metal ions including Ag(I), Zn(II), Cd(II), Hg(II), Co(II), Cu(II), and Fe(III) chelating with CRT, and this characteristic property can be used for the quantitative determination of CRT [30,31]. The production of a soluble Cu–CRT combination on the copper electrode provided the basis for the development of an amperometric method for measuring CRT. The oxidative current formed during the reaction is related to the CRT concentration [31].

Due to its high specific surface area, low cost, low toxicity, and electro-catalytic activity, copper (II) is an appealing alternative material to increase the sensitivity of electrochemical detection towards CRT [32]. One-dimensional CuNWs act as highly efficient electron transport channels, offering high conductivity and a large surface area [33], making them integral to improving the electrochemical performance and sensitivity of advanced sensor systems [34,35]. CuNWs are prominent for their high conductivity, affordable precursor cost, and potential integration with a well-known dual damascene system [36,37]. MoS_2 nanomaterials have been exclusively investigated for their potential applications in diagnostic and biomedical applications. These applications encompass the detection of various biomolecules such as dopamine (DA), ascorbic acid (AA), glucose, and biomarkers [38]. MSQD has been selected for the selective detection of CRT. MSQD belongs to the highest class of transition metal dichalcogenide (TMDC) family with practical electrical, mechanical, and chemical properties. They possess a high surface-to-volume ratio and increased active edges which enhance the catalytic properties of MSQD [39].

Herein we develop a non-enzymatic method to detect CRT via the formation and electrochemical detection using CuNW/MSQD complex. Under optimal conditions, the developed sensor exhibits a good linear range over the concentrations and in the presence of other interfering substances. Along with the creation of the novel electrochemical sensor, the detailed electrochemical behavior of the CuNW/MSQD complexes was also explored. In this study, we tested real urine samples and compared them with laboratory results this could reflect the performance of the developed sensor which may be reflected in laboratory to practical applications. Moreover, machine learning (ML) algorithms were applied to quantify CRT by training and testing in a large pool of experimental data. Fig. 1 schematically illustrates the summary of stages involved in the present work. Thus, our methodology provides a simple, low-cost, and sensitive technique to develop a biosensor for CRT detection.

2. Experiments

2.1. Reagents and chemicals

All chemicals were of analytical quality grade and used without any purification. All samples were prepared in phosphate buffer (K_2HPO_4 ($\geq$ 99 % purity) and KH_2PO_4 (99 % purity), and all were purchased from Sigma-Aldrich, India. Dopamine hydrochloride (DA) (>99.5 % purity), uric acid (UA) (>99.6 % purity), ascorbic acid (AA) (>99% purity), dimethylformamide (DMF (99.8 %), and bulk crystals of MoS_2 (6 μm), were from Sigma Aldrich Chemical Company, India. CRT was purchased from Merck Chemicals, India. Sodium hydroxide (NaOH), ethylenediamine (EDA) (99 %), hydrazine (N_2H_4) (98 %), and copper nitrate ($Cu(NO_3)_2$) (99.7 %) were purchased from Sisco Research Laboratories Pvt. Ltd. India. All aqueous solutions were prepared using deionized water from a Milli-Q system (18.3 MΩ Millipore). Further 0.1 M phosphate buffer solution (PBS pH 7.0) was used as a supporting electrolyte throughout the experiment.

2.2. Surface characterization

The surface morphology of the modified carbon electrode was analyzed using field emission scanning electron microscopy (FESEM) (model: JEOL JSM 7200F FESEM, Japan). Raman spectroscopy was taken using BRUKER RFS 27 MultiRAM FT Raman Spectrometer (Germany) with 4000–50 cm^{-1} spectral range (Laser source −1064 nm). The crystallographic structure of products was determined with X-ray powder diffraction (XRD) spectrum (Rigaku Smartlab 3KW, Japan) which uses a Cu-Kα source with a wavelength of 1.540564 Å. The UV–visible spectra were recorded on a UV-spectrophotometer (PerkinElmer, Lambda 35, USA), and photoluminescence (PL) measurements were taken using a JASCO spectrofluorometer (FP- 8300, Japan).

2.3. Synthesis of CuNW

Herein we synthesized CuNW with an aqueous reduction route at low temperature. EDA was employed as a growth-directing agent and hydrazine as a reducing agent during the solution-based synthesis of CuNWs. The synthesis method is similar to those found in works of published literature [40]. Briefly, a process involved the mixing of copper nitrate solution (0.1 M in 2.0 mL DI water) with aqueous NaOH solution (15 M in 40 mL DI water). The solution was added to a glass reactor (capacity 50 mL). EDA (0.1 M, 266 μL) and hydrazine (5.72×10^{-3} M, 21 μL) were also added sequentially, followed by thorough mixing of all reagents for 3 min. The reactor was then placed in a water bath at 60 °C temperature. After 45 min, the solution changed to a clear solution containing a reddish-brown precipitate. The obtained CuNW were collected and washed several times with DI water and ethanol, and finally stored in ethanol solvent to prevent further oxidation.

2.4. Synthesis of MSQD

The MSQD was synthesized from bulk MoS_2 crystals from the reported method in the literature [41]. MoS_2 crystals (0.5 g) were mixed with 250 mL of DMF, and this mixture was homogenized using a high-shear mixer at 8000 rpm shearing rate for 3 hours in a water bath by maintaining 100 °C and the shearing system led to the formation of well-dispersed QDs. The final product was collected and it has been identified that they are highly dispersed in DMF and further, it is characterized using various characterization techniques.

2.5. Fabrication of the sensor

First, 500 μL of MSQD was used to dissolve 0.5 mg of CuNW to prepare the suspension. Subsequently, the suspension was homogenized for one hour using ultrasonication. The homogenous suspension (5 μL) was immobilized on a well-polished glassy carbon electrode (GCE) surface by physical adsorption via the drop-casting method. Before drop casting CuNW/MSQD on GCE, the electrode was polished with 0.05 μM alumina slurry and washed with DI water several times. The drop-casted electrode was dried under ambient conditions.

2.6. Electrochemical measurements

Electrochemical techniques such as Cyclic Voltammetry (CV), Differential pulse Voltammetry (DPV), and electrochemical impedance spectroscopy (EIS) performed using single-channel Palmsens electrochemical potentiostat (Emstat4HR Electrochemical potentiostat) interfaced with PSTrace software were utilized for validating the sensing performance. For the measurements a typical three-electrode system consists of a GCE as the working electrode (3 mm), Ag/AgCl (3 M KCl) as a reference electrode, and a Pt wire as a counter electrode used for voltammetric studies. The pH measurements were carried out using a pH meter (Systronics pH meter).

Electrochemical characterization of the fabricated sensor CuNW/MSQD/GCE was carried out using *CV* and EIS in a redox mixture containing 5 mM $[Fe(CN_6)]^{3-/4-}$ in 0.1 M phosphate buffer solution at pH 7.0. *CV* was recorded in the potential range of - 0.2 V to 0.6 V at the scan

Table 1
Details of human urine sample analysis.

Sample	Dilution Factor (x)	Spiked CRT (μM)
A	20	502.46
	50	265.26
	100	186.20
B	20	159.40
	50	128.04
	100	117.59
C	20	172.03
	50	133.09
	100	120.12

rate of 100 mV/s. EIS was recorded at the redox probe's half-wave peak potential using frequency scanning from 100 kHz to 100 mHz and frequency analysis. The voltammetric behavior of CRT, UA, DA, and AA was studied using DPV in the potential range between −0.2 V to 0.8 V at a scan rate of 50 mV/s. Appropriate aliquots of the analyte solutions were added after running the DPV in the buffer, and DPVs were recorded after each addition to obtain calibration plots. Minimum and maximum ranges of CRT, UA, DA, and AA in serum samples were also detected electrochemically. All voltammetric studies were carried out in 0.1 M phosphate buffer solution (pH 7.0) at room temperature.

The complex mixture analysis was done by injecting different concentrations of the interfering molecules such as AA, DA, dUA, and CRT, the operated electrode's selectivity to CRT was confirmed against other interfering molecules**.** The analysis was carried out with lower and higher concentration ranges of biomolecules. DPV studies were carried out with a lower range of AA (1.76 μM), higher range of AA (22.72 μM), a lower range of DA (3.26×10^{-7} μM), a higher range of DA (1.96×10^{-5} μM), a lower range of UA (11.89 μM) and a higher range (47.58 μM) of UA as an interfering molecule with consecutive addition of CRT from 1.96 μM to 966.0 μM in 0.1 M phosphate buffer (pH 7.0) from −0.2 *V*to 0.8 V.

2.7. *Real sample analysis*

Fresh urine samples were collected from three healthy *v*olunteers for the determination of CRT. The three urine samples' CRT levels were tested on Apollo diagnostics by the modified Jaffe, kinetic method and the results (8855.26 μM, 1170.68 μM, and 1453.62 μM) were compared with the experimental values. To eliminate the protein from the fresh urine sample, two times as much acetone (*v*/v) was added. After centrifugation of the sample acetone was removed. Subsequently, the sample was diluted to 100-fold, 50-fold, and 20-fold with phosphate buffer solution having pH 7.0, and analysis for the CRT detection was performed (Table 1). A clinical analysis was also done for the determined samples, and the results were compared. There is another combination of data acquisition which was done in spiked concentration of CRT in known concentration of urine samples.

2.8. *Quantification of CRT in complex mixture and urine samples*

Analysing electrochemical data recorded from biofluids has been the most challenging task in recent times due to its complexity of overlapping, and interfering electrochemical signatures generated from the redox-active species. Here, we have used four datasets in this analysis of the quantification of CRT in real samples. The four datasets are related to the data recorded using bare (GCE) and modified (CuNW/MSQD) electrodes from differently diluted urine samples. There is another dataset where the urine samples were spiked with known CRT concentrations which was recorded using modified electrodes. The last dataset that we combined here is the complex mixture data set as recorded using modified electrodes in the above sections. This strategy was followed here to have a large data set, an important metric to follow in ML-related data analysis, and most importantly to accommodate the huge variance in the dataset to simulate the real case scenario. In this research, a strategic combination of all four datasets was undertaken to conduct diverse analyses. Each data set from real samples with specific features related to electrical and chemical properties was integrated with the 'complex mixture' dataset, which provided a detailed exploration of chemical compositions. The variations in features across datasets allowed for a comprehensive investigation into the predictive modeling of concentration levels under different conditions. Each combination served a distinct purpose, contributing unique insights to the overall research. This strategic integration of diverse datasets aimed to enhance the depth and breadth of the analysis, shedding light on the multifaceted factors influencing concentration predictions in the study. Please find the details of data organization for different cases and preprocessing in the supplementary section. The experiments were performed on the TensorFlow-2 framework having Python 3.7.13 over a computer with Intel(R) Xeon(R) CPU @ 2.00GHz having 52 GB RAM and Tesla T4 16 GB GPU.

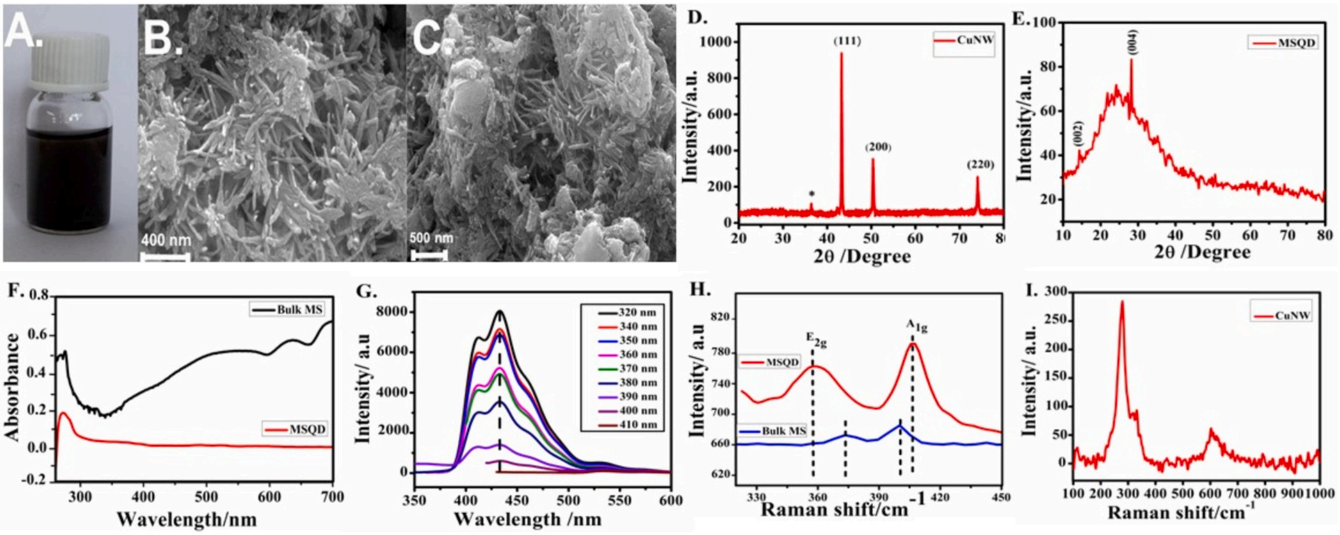

Fig. 2. (A) Optical image of well-dispersed CuNW in ethanol, (B and C) FESEM images of as-synthesized CuNW and CuNW/MSQD, (D and E) XRD pattern of CuNW and MSQD. (F) U*V*–vis absorption spectra of MSQD and bulk MS, (G) PL spectra of MSQD, and (H and I) Raman spectra of MSQD, bulk MS, and CuNW.

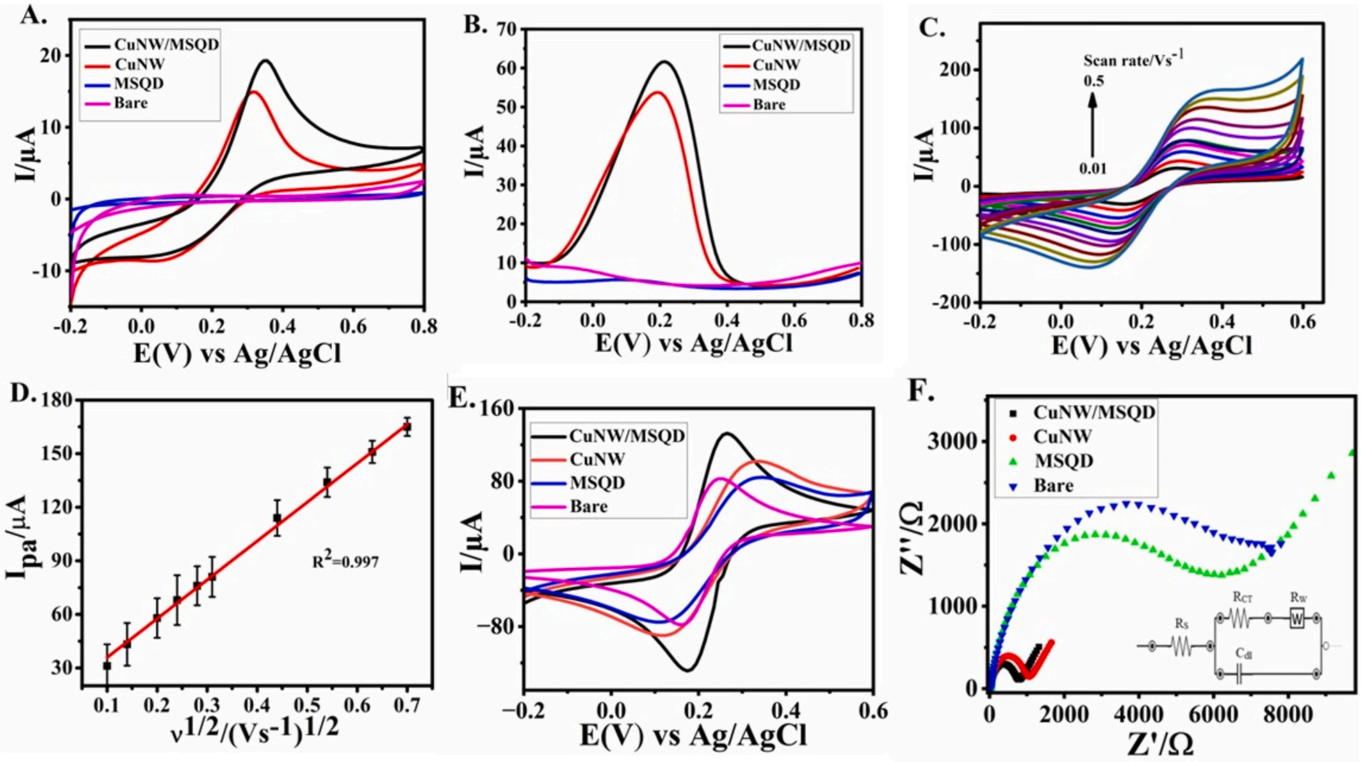

Fig. 3. (A) CVs and (B) DPVs were obtained by chemically modified materials on GCE for the detection of 0.28 mM CRT in 0.1 M phosphate buffer solution (pH 7.0) having the potential of −0.2 V to 0.8 V, at the scan rate of 50 mVs^{-1} (C) Recorded CVs of redox couple 5 mM $[Fe(CN)_6]^{3-/4-}$ at the scan rate of 10 mVs^{-1} to 500 mVs^{-1} using CuNW/MSQD modified GCE (D) The linear plot shows the linear dependence of the recorded current peak Vs. square root of scan rate. CVs (E) and the Nyquist plots (F) (Inset: equivalent circuit used for fitting) were recorded for bare, CuNW/GCE, CuNW/MSQD/GCE, and MSQD/GCE.

3. Results and discussion

3.1. Material characterization

3.1.1. Morphological characterization

The morphology of prepared three samples CuNW, MSQD, and CuNW/MSQD were characterized by FSEM. Fig. 2A shows the dispersion of CuNW in ethanol solution and Fig. 2B and C show FESEM images of CuNws and CuNW/MSQD respectively. It is interesting to note that the prepared nanowire cake rises to the top of the solution. The complete absence of the light blue color in this process indicates the reductive conversion of Cu^{2+} ion complexes to metallic copper and now the solution turned red in color and is completely dispersed in ethanol solution. The synthesized CuNW are straight manner and smooth, particle-free surfaces as shown. It is shown CuNW/MSQD composite depicts long crystalline nanowires.

3.1.2. XRD analysis

X-ray diffraction analysis was used to determine the phase purity and crystalline nature of synthesized CuNW and MSQD. The crystallographic structure and purity of prepared CuNW are confirmed by XRD patterns. The XRD of CUNWs shows a typical face-centered cubic structure (fcc). Three main Cu peaks were observed from the XRD pattern (Fig. 2D) of CuNW. The typical diffraction peaks (2θ) positioned at 43.4^0, 50.2^0, and 74.3^0. Compared with the standard peak positions of CuNW (JCPDS -04-0836) all observed peaks are assigned to (111),(200), and (220) planes. A minor peak at 36.1^0 corresponding to the (111) plane is due to the oxidation of CuNW (The * symbol in Fig. 2D represents the [111] plane of Cu_2O) [42]. The XRD pattern of MSQD (Fig. 2E) shows characteristic diffraction peaks (2θ) which were located at 14.4^0, $28.5^{0,}$ and 35.7^0 and were assigned to (002), (004), and (102) planes respectively (JCPDS-00-037-1492). Since the material is very thin or has a few layers, it reveals no intense interference on the crystal plane. so, this XRD graph shows a very thin layer phase of quantum dots [43].

3.1.3. Spectroscopic study of MSQD

The UV–vis absorption spectra of bulk MoS_2 and MSQD are shown in Fig. 2F. The absorption spectra of bulk MoS_2 show three characteristic peaks. The peaks at 626 nm and 682 nm are because of the transition from the valence band to the conduction band at the K point the broad peak at 495 nm is assigned for the transition from the valence band to the conduction band and the Brillionzone M point [44]. These characteristic peaks disappeared in MSQD spectra. In the spectrum of MSQD only one peak was observed in the UV region ($\lambda \sim 273$ nm) can be explained by the excitonic features of QDs [43]. However, in the case of QDs, it is evident that the bandgap is opening up, shifting, and broadening the excitonic transitions Blueshift also can be explained through the quantum size effect [43,44]. These are the characteristics of the production of quantum dots because of the expansion of the energy gap in the Brillouin zone's K point [41]. The photoluminescence (PL) spectral study of the MSQD suspension was measured at various excitation wavelengths, as shown in Fig. 2G. The PL spectra show a strong emission peak at 432 nm under the excitation wavelength from 320 nm to 410 nm. The additional peaks in the spectra are attributed to the vibronic coupling to the vibrational modes at high frequencies, which could originate from the edge bonds present in QDs [29]. The data reveals the dependence of PL emission peak intensities on the size of MSQD. As the size of the QDs increases, the strength of the emission peak diminishes [45]. These are typical PL features that rely on size. The excitation-dependent PL characteristic revealed the polydispersity of the MSQD in their as-prepared state [46,47].

3.1.4. Raman spectroscopy

The synthesized MSQD was characterized by Raman spectroscopy.

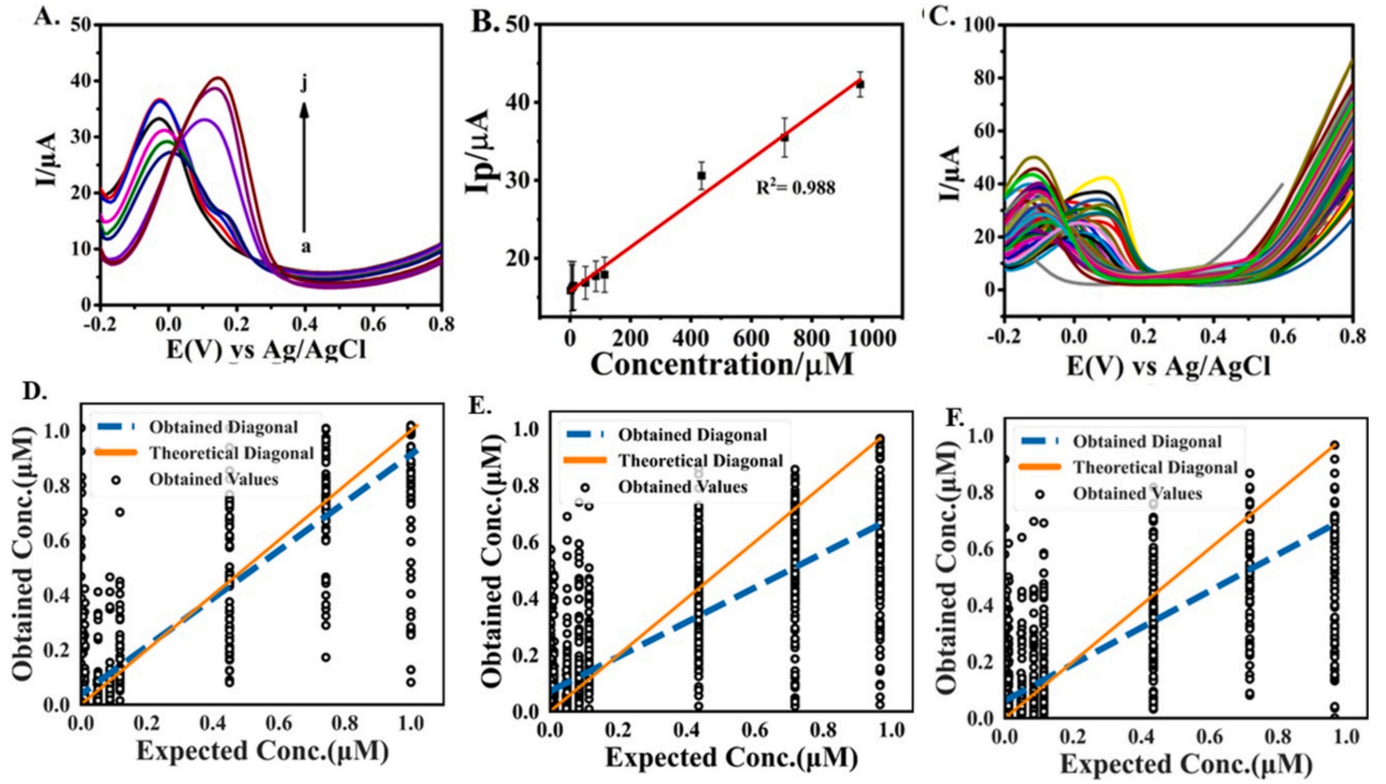

Fig. 4. (A) DP*V* obtained for 1.96–966.0 μM concentration of CRT in 0.1 M phosphate buffer solution (pH 7.0) within a potential window of −0.2 V to 0.8 V, at the scan rate of 100 mVs^{-1} and 'a to J' represents 1.96, 6.54, 10.7, 50, 84.8, 114, 717, and 966.0 μM concentration of CRT (b) linear calibration graph showing the linear relationship of the current peak vs concentration of the analyte (C) DPV recorded by CuNW/MSQD modified electrode in the absence and presence of interference at the potential of −0.2 V to 0.8 V. Regression plots for the prediction of CRT combined data set recorded from the complex mixture using (D) ANN, (E) RF, and (F) KNN regressors.

Due to its high sensitivity and non-reactivity of the sample, Raman spectroscopy has been used extensively for studying the vibrational characteristics of transition metal dichalcogenides [48]. Raman spectra of bulk MoS_2 are shown in Fig. 2H in which two peaks E_{2g} and A_{1g} at 374 cm^{-1} and 400 cm^{-1} respectively. The Raman spectra of MSQD (Fig. 2H) show two prominent characteristic peaks at 359.1 cm^{-1} and 407 cm^{-1} corresponding to E_{2g} (in-plane optical vibration) and A_{1g} (out-of-plane optical vibration) active modes respectively. Where E_{2g} vibration includes both Mo and S atoms and A_{1g} includes only S atom [49]. Compared to bulk, MS, the A_{1g} vibration of MSQDs blue shifted from 400 cm^{-1} to 407 cm^{-1} and the E_{2g} vibration is red shifted. Usually A_{1g} vibration blueshifts with increased sample thickness from monolayer to bulk [44].Raman spectra of CuNw which are oxidized after exposure to the atmosphere are shown in Fig. 2I. The Raman peaks of nanowires can be observed peaks at 288, 330, and 621 cm^{-1} [50]. The Raman peaks get stronger, sharper, and slightly shift to a higher wavenumber as the grain size rises [46].

3.2. *Electrochemical characterization*

CV was conducted to know the fundamental electrochemical characteristics of CRT at the bare and different modified electrodes in 0.1 M phosphate buffer solution (pH 7.0) with forward scan ranged potential range from −0.2 V to 0.8 V at a scanning rate of 50 mVs^{-1} as shown in Fig. 3A and DPV are shown in Fig. 3B. In the CV, oxidation of CRT at CuNW/MSQD reveals a reversible oxidation peak at 0.34 V with peak current (Ip) 19.47 μA which is a higher current than CUNW modified and MSQD modified electrodes, and no such kind of oxidation peak was observed for bare electrode. To confirm the results, DPV was also performed, showing that the CuNW/MSQD modified electrode exhibited a higher current of 61.45 μA compared to other modified electrodes. The enhancement in the sensor's signal is facilitated by the synergistic properties of the CuNW/MSQD. During the electrochemical detection, the CRT molecule will adsorb onto the surface of the CuNW/MSQD-modified electrode. It involves highly conductive Cu form complexes with CRT on the surface of MSQD [51], and the charge transfer followed from CUNW- CRT complexes to MSQD [52]. It results in the selective and efficient oxidation of CRT molecules. Furthermore, the active edge sites and higher surface area of MSQD, facilitate selective interaction with Cu-CRT molecules, reducing interference from other compounds such as DA, UA, and AA [38].

Based on this, it is confirmed that the CuNW/MSQD compound shows the highest current. This indicates that the electrochemical activity of the modified electrode surface can be enhanced by the addition of CuNW and MSQD to the surface than any other electrodes. The electrochemical activity of the CuNW/MSQD modified electrode was characterized.

3.2.1. *Effect of scan rate*

To expand the investigation on the effective surface area of the modified electrode, a scan rate or speed study was investigated in 5 mM ferro/ferricyanide solution at a scan rate from 10 to 500 mVs^{-1}. The recorded CVs for the redox couple ferro/ferricyanide displayed similar cathodic and anodic waveform shapes for the CuNW/MSQD modified GCE (Fig. 3C) electrode were shown. Fig. 3C shows the effect of the scan rate (on the electrocatalytic anodic peak current (I_{pa}) of the modified electrode. As the scan rate increases from 10 mVs^{-1} to 500 mVs^{-1} the anodic peak current enlarged, and the peak potentials are shifted negatively indicating the reaction nature is reversible. The relationship between peak current and square root of scan rate was plotted for CuNW/MSQD modified GCE electrode (Fig. 3D) and the Plot gives a good linear relationship (R^2 = 0.997). It indicates the diffusioncontrolled reaction of CRT at the CuNW/MSQD electrode-electrolyte interface.

3.2.2. *Electrochemical properties of CuNW/MSQD/GCE*

Using CV and EIS the electrochemical behavior of the sensor at various stages has been analyzed in the presence of Fe-redox couple $[Fe(CN)_6]^{3-/4-}$and obtained voltammogram shown in Fig. 3E. From the figure it is observed that CUNW/MSQD-modified electrode shows higher peak current than CUNW-modified and MSQD-modified electrodes. The significantly higher peak current exhibited by the CuNW/MSQD -modified electrode in the $[Fe(CN)_6]^{3-/4}$ demonstrates the composite's superior electrochemical properties, attributed to its enhanced conductivity, catalytic activity, and charge transfer efficiency. These findings affirm the effectiveness of the CuNW/MSQD composite for the detection of CRT. The effective surface area (A_{eff}) can be calculated using the Randles–Sevcik Eq. [53].

$$I_p = 0.4463\ (F^3/RT)^{1/2}\ n^{3/2} A_{eff}\ D^{1/2} C^{*3/2}\ \nu^{1/2} \tag{1}$$

Where I_p is the peak current (A), F is the Faraday's constant (96,485.339C/mol), R is the universal gas constant (8.31447 $J\ K^{-1}\ mol^{-1}$), T is the absolute temperature (K), n is the number of electrons transferred in a redox cycle ($n = 1$ for a ferro/ferricyanide reaction), A_{eff} is the effective electrode surface area in working (cm^2), D is the diffusion coefficient of electroactive compound($cm^2 s^{-1}$) [$(0.72 \times 10^{-5}\ cm^2\ s^{-1}$ for ferricyanide and $0.67 \times 10^{-5}\ cm^2\ s^{-1}$ for ferrocyanide], C* is the molar concentration of electroactive species (mol cm^{-3}) and ν is the scan rate (Vs^{-1}). surface area (A_{eff}) has been calculated for bare GCE is $9.1 \times 10^{-3}\ cm^2$ and for CuNW/MSQD/GCE is $17.2 \times 10^{-3}\ cm^2$. The modified electrode exhibits a larger surface area compared to the bare GCE, which boosts its capacity for electron transfer. This implies that the modification of bare GCE with conductive CUNW/MSQD enhanced the peak current for the electrochemical analysis of CRT with high sensitivity and rapid response rate.

Further, the kinetics of electron transfer for the modified electrode was studied through EIS. The EIS is a useful technique for examining the characteristics of the electrode-solution interface and the effectiveness of charge transfer between the electrode interface and the analyte-containing solution. Nyquist plots along with the equivalent circuit were shown in Fig. 3F. The diameter of the semi-circle indicates charge transfer resistance (R_{CT}). Bare GCE shows higher charge transfer resistance than MSQD, CuNW, and CuNW/MSQD electrodes. This indicates that the embedding of CuNW with MSQD increases the charge transfer characteristics of MSQDs. Upon fitting the impedance spectra with the suitable equivalent circuit (Inset: Fig. 3F), the charge transfer resistance value (R_{CT}) value for bare, MSQD, CuNW, and CuNW/MSQD modified electrodes were found to be 1002 Ω 986.9 Ω, 676.1 Ω, and 564.2 Ω respectively. The combination of CUNW/MSQD results in the lowest R_{CT} value, it reflects the enhanced electron transfer and catalytic activity compared to the bare and other modified electrodes. The impedance R_{CT} values are in accordance with the diffusion currents of CVs.

3.2.3. *Electrochemical analysis of CRT in buffered samples and in the presence of interfering species (complex mixture)*

DPV is frequently employed as a sensitive technique to investigate the impact of varying CRT concentration (1.96 to 966.0 μM) in phosphate buffer pH 7.0 at 0.1 V/s using the CuNW/MSQD sensor on the peak current (Fig. 4A). The recorded voltammogram shows the characteristics of increased current densities with increased concentrations. The anodic peaks are getting a higher value of current at 966.0 μM concentration. The modified electrode detects from 1.96 to 966.0 μM concentration of CRT. The peak is gradually shifting positively with increasing concentration. This may be due to the oxidation reaction of CRT. The corresponding calibration graph shows linearity with a 0.988 R^2 value as shown in Fig. 4B. The linear equation is represented as;

$$I_{P(CRT)} = (0.028 \pm 0.001)\ [CRT]_{\mu M} + (15.795 \pm 0.448)\ (R^2 = 0.988) \tag{2}$$

From Fig. 4B limit-of-detection (LOD) and sensitivity were calculated as 0.92 μM and 0.028 which shows that the modified electrode allows the detection of CRT levels in a highly sensitive manner in buffered samples. Recent studies reported on electrochemical detection of CRT are listed in Table 5. The developed electrochemical sensor's linearity range and LOD for CRT determination are evaluated in comparison with values reported in the literature (Table 5). It is evident from the comparison that the developed sensor shows a wide linearity range and other analytical parameters that are on par with the literature. Moreover, the LOD is notably low.

Further, the CRT detection was investigated in the presence of major interfering species (e.g. DA, AA, UA) and it was found that the CRT electrochemical signature is influenced by the presence of these interfering species generating highly complex electrochemical signature where it becomes challenging to deconvolute the electrochemical signature of CRT from complex electrochemical signatures (Fig. 4C). The impact of individual interfering species and the resultant electrochemical signature can also be seen in Fig. S1, S2, and S3 of the supplementary information. The electrochemical signature of CRT is interfered with and masked by the presence of the interfering species generating overlapping electrochemical signatures which depends on many factors, e.g. activity of the electrode towards the interfering molecules along with CRT generating a partially selective electrochemical signature, and concentration of individual molecules and their resulting impact on the electrochemical signature generating convoluted electrochemical signature. These issues become more prominent in the case of biofluids where there are many molecules present in the solution generating even more complex electrochemical signatures. Since the problem of complex electrochemical signature has many facets and therefore, it cannot be handled by simple linear fitting, and it requires some multivariate statistical approach to handle such a complex electrochemical data set. Therefore, we decided to use ML methods to process the complex electrochemical data recorded using CuNW/MSQD. The analysis of complex mixtures is framed as a regression problem, employing various ML regressor models such as Artificial Neural Network (ANN) [54], Random Forest (RF) [55], and K-Nearest Neighbor (KNN) [56]. The details of the employed data set can be found in the supplementary file under section 2. Data Analysis using ML, where we have also provided the feature details and correlation analysis among selected features. Fig. 4 (D), (E), and (F), show the regression plots for predicting CRT concentration from a complex mixture using ANN, RF, and KNN regressors, respectively.

The details of the applied models are as below:

ANN-based analysis: Before applying the ANN model to the complex mixture data set, preprocessing is conducted. Label encoding is performed on the categorical feature '*chemical*', converting its categories into numerical values. Next, outlier detection and removal are applied [57]. We also use min-max normalization to normalize the data [58]. The dataset is now distributed into 7 input features ('*potential*' *('V')*, '*current*', '*chemical*', '*anodic_potential*', '*anodic_current*', '*cumulative_min_current*', and '*cumulative_min_V*'), and 1 output feature ('*concentration*'). Therefore, the employed ANN architecture has 7 neurons in the input layer. Here, the ANN consists of 10 sequential hidden layers consisting of 64, 128, 256, 512, 712, 1024, 712, 512, 256, and 128 respective neurons with ReLU (Rectified Linear Unit) activation functions. The output layer consists of a single neuron with a linear activation function, indicating a regression task. This layered structure is selected to incrementally abstract data features into higher dimensions, with the hypothesis that this configuration enhances the model's ability to capture and generalize complex patterns. We use Adam for optimization and mean squared error as a loss function. The training and testing data is in the ratio of 70:30. For model validation, we use 20 % of the training data. We perform the model training for 3000 epochs with

Table 2
Analyses from various ML models for training and testing on Complex mixture.

Algorithm	MAE	MSE	RMSE	NRMSE	R^2	LOD (µM)	LOQ (µM)
ANN	0.071	0.024	0.155	0.663	**0.831**	2.2716	7.5721
RF	111.26	36,903.4	192.1	0.915	**0.691**	4.4933	14.977
KNN	109.03	37,507.8	193.66	0.933	**0.679**	4.3280	14.426

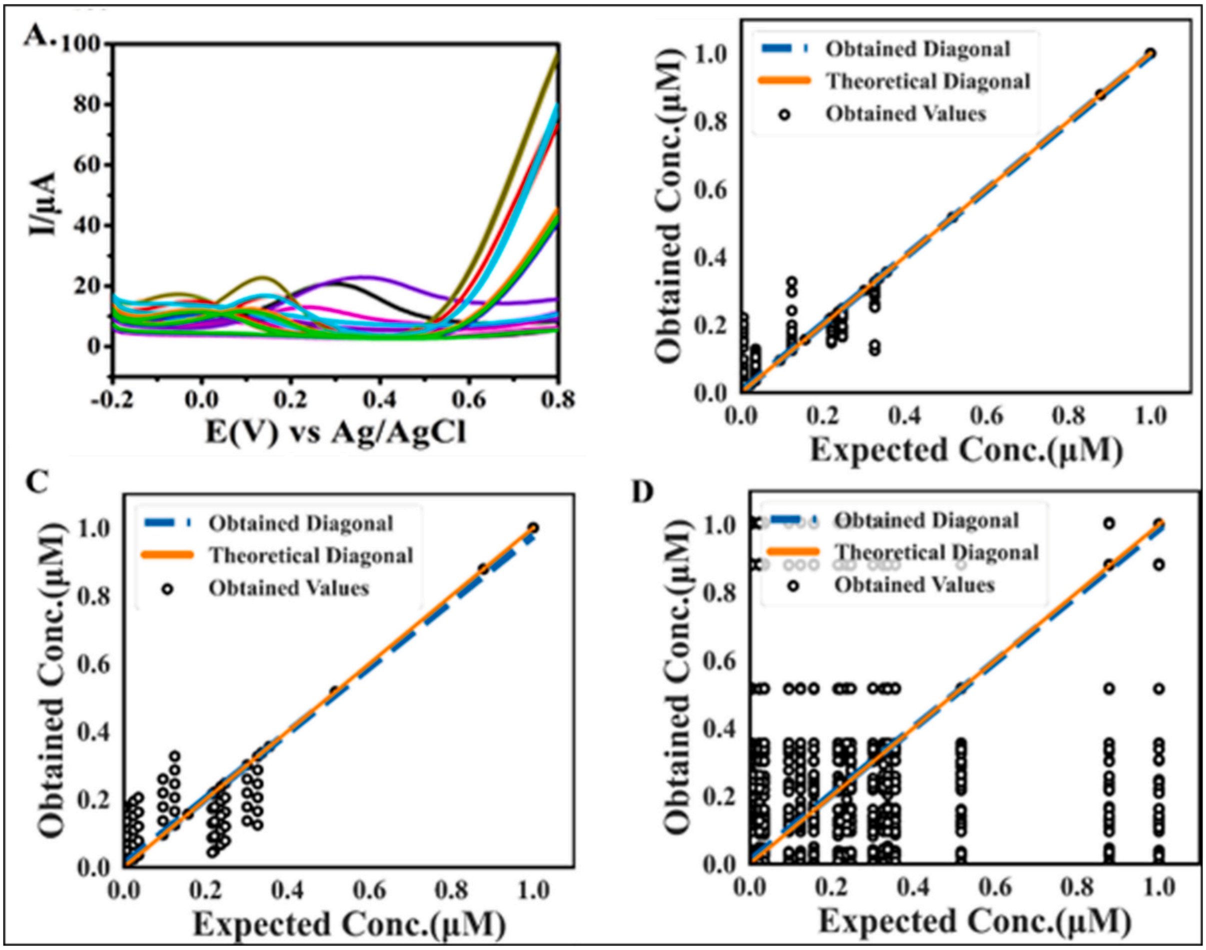

Fig. 5. (A) DPV recorded for the detection of CRT in human urine samples. Regression plots for training/ testing on urine data from (B)RF, (C) KNN, and (D) ANN regressors respectively.

mini_batch_size = 30.

RF-based analysis: Here, we maintain the same 7 input features and 1 output feature as previously mentioned in the ANN-based analysis. The training, testing, and validation sets remain the same as those used in the ANN-based analysis after outlier removal and normalization. Here, we perform the hyperparameter tuning using randomized search, fitting for 3 folds for every 100 candidates, and set n_estimators = 1733, min_samples_split = 2, min_samples_leaf = 1, max_depth = 100. We use bootstrap aggregating to reduce overfitting. Here we engage squared loss. The remaining hyperparameters are maintained at their default settings, as per the Scikit-learn library [59].

KNN-based analysis: Similar to the ANN and RF-based analyses, we use the pre-processed data, maintain the same input and output features, and keep the training, testing, and validation sets consistent. Based on the validation set performance, we tune the hyperparameters and fix n_neighbors = 5, leaf_size = 30. We here use Euclidean distance,kd-tree, and uniform weights without favoring closer neighbors to compute nearest neighbors. The remaining hyperparameters are kept at their default settings, as specified by the Scikit-learn library [59].

We employed various performance metrics to evaluate our models, including Mean Absolute Error (MAE), which measures the average absolute differences between predicted and actual values, and Mean Squared Error (MSE), which calculates the average of the squares of these differences. The Root Mean Squared Error (RMSE) represents the square root of the MSE, providing a measure of the average magnitude of the errors. The Normalized Root Mean Squared Error (NRMSE) normalizes the RMSE by dividing it by the range of the dependent variable. Additionally, the R-squared (R^2) metric measures the proportion of the variance in the dependent variable that is predictable from the independent variables. Lastly, the LOD represents the lowest concentration of analyte that can be reliably detected but not necessarily quantified, and the Limit of Quantification (LOQ) is the lowest concentration of an analyte that can be quantitatively detected with acceptable precision and accuracy. In Table 2, we present the performances of ANN, RF, and KNN regressors with respect to the above metrics. We obtained R^2 of 0.831, 0.691, and 0.679 from ANN, RF, and KNN, respectively. From this table, we can comprehend that overall, ANN performed better than RF and KNN. From the analysis of CRT in complex mixtures, it is concluded

Table 3
Analyses from various ML models for training and testing on Urine.

Algorithm	MAE	MSE	RMSE	NRMSE	R^2	LOD (μM)	LOQ (μM)
ANN	0.275	0.149	0.034	0.134	**0.984**	0.003	0.012
RF	0.004	0.001	0.017	0.068	**0.996**	0.001	0.003
KNN	0.019	0.002	0.047	0.184	**0.970**	0.007	0.024

that we can quantify the levels of CRT in the presence of interfering species generating overlapping and masking electrochemical signatures.

3.2.4. Electrochemical analysis of CRT in urine samples using ML

After the quantification of CRT in complex mixture solutions, we validated the performance of our sensors and ML models in urine samples. Here, we have used the electrochemical data set recorded using bare and modified electrodes to accommodate the variability and cross-reactivity from both electrodes which in a result generates variable electrochemical signatures suitable for training and testing of ML (Fig. 5). To improve the predictive performance of a ML model for estimating concentration, we enhanced the feature set. Initially, the input features included '*potential*' ('*V*'), '*current*' (*I*), '*number_of_folds*', and '*sample_name*', with '*concentration*' as the output feature. To augment this dataset, we engineered additional features*:* '*anodic_potential*', '*anodic_current*', '*cumulative_minimum_I*', and '*cumulative_minimum_V*'. The feature engineering details can be found in the supplementary file in section 2 of Data Analysis using ML. Anodic potential and current capture the electrochemical properties during anodic reactions, while cumulative minimum current and potential provide insights into the minimum values observed over time, potentially reflecting stability and reaction thresholds. By integrating these new features, we aimed to capture more detailed patterns in the electrochemical data, thereby improving the model's ability to predict concentration accurately. Our results showed a significant improvement in predictive performance, demonstrating the importance of these engineered features in enhancing the model performance. Here, we also performed preprocessing, including outlier removal and data normalization, as a complex mixture [57,58].

ANN-based analysis: The input layer of ANN contains 8 neurons due to having 8 abovementioned input features ('*V*', '*I*', '*number_of_folds*', '*sample_name*','*anodic_potential*', '*anodic_current*', '*cumulative_minimum_I*', and'*cumulative_minimum_V*'). It contains 1 neuron in the output layer for predicting *concentration*. The ANN comprises 10 sequential hidden layers consisting of 64, 128, 256, 512, 512, 256, 256, 128, 64, and 32 neurons, respectively, with ReLU activation. Here also, we use Adam for optimization and mean squared error as a loss function. Similar to the complex mixture, we split training and testing data in a 70:30 ratio, and engage 20 % of the training data for validation. Here the ANN model is trained for 1000 epochs and performs the training batch-wise with a mini-batch size equal to 50.

RF-based analysis: We here maintain the same 8 input features and 1 output feature; the training, testing, and validation sets remain the same as the above-mentioned ANN-based analysis. Here, we use the same hyperparameters [55,59] as fixed in the RF-based analysis of complex mixtures except for n estimators = 100, and random_state = 42.

KNN-based analysis: Similar to the above ANN and RF-based analyses, we use the preprocessed data, maintain the same input and output features, and keep the training, testing, and validation sets consistent. The hyperparameters are set as of KNN-based analysis of the above complex mixture [56,59].

We utilized various performance metrics to assess the efficacy of our models in the electrochemical analysis of CRT in urine samples. Table 3 presents the performances of ANN, RF, and KNN regressors with respect to MAE, MSE, RMSE, NRMSE, R^2, LOD, and LOQ. We obtained R^2 of 0.984, 0.996, and 0.970 from ANN, RF, and KNN, respectively. This table comprehends that all these models performed quite similarly; however, RF performed better than ANN and KNN regressors. From the analysis of CRT in urine samples using the bare and modified electrode data sets, it is found that the CRT levels can be detected even below the therapeutic range. In the complex mixture data analysis above, only the modified electrode data set was used due to its better response in buffered samples and complex mixtures, However, for CRT analysis in urine samples, both bare and modified electrode's data have been used accommodating the larger variability of the data set resulting in an improved model performance and therefore better LOD and LOQs for different models.

3.2.5. Electrochemical analysis of CRT in complex mixture and urine samples combined using ML

In this analysis, a combined data set of the above two analysis (complex mixture and urine) was used to accommodate maximum variability in the data set and to simulate the real-time scenarios where we will have a larger pool of data collected from different individuals with different metabolic profiles resulting in a variable background current as well as response. The real-time scenario is even more complex than this where the data variability will have many facets, where all the factors such as e.g. gender, geography, lifestyle, smoker or drinker, food habits, and preexisting medical conditions contribute to different electrochemical profiles. Here, we tried to simulate such variable electrochemical responses recorded using the bare and modified electrodes in different solutions by combining both the electrochemical data sets as analyzed above. Additionally, the objective was to develop a robust predictive model for predicting concentration in a highly variable electrochemical data set. The details of the dataset can be found in the supplementary file. Here also we performed the preprocessing, i.e., outlier removal and normalization. Initially, the input features included '*potential*' ('*V*'), '*current*' ('*I*'), and '*chemical*'. Feature engineering techniques were applied to derive 8 new features such as '*resistance*', 'E_{pa}' ('*anodic_peak_potential*'), 'E_{pc}' ('*cathodic_peak_potential*'), 'I_{pa}' ('*anodic_peak_current*'), 'I_{pc}' ('*cathodic_peak_current*'), '*PS*' ('*peak_potential_separation*'), '*pH*' ('*peak_height*'), '*half_wave_potential*' values from existing data columns.

ANN-based analysis: The employed ANN architecture comprises an input layer tailored to 11 abovementioned features, followed by 13 hidden layers arranged sequentially with 64, 1024, 512, 512, 512, 512, 256, 128, 128, 128, 64, 64 neurons, respectively. Here also, we use ReLU activations to introduce non-linearity. The output layer includes a single neuron with a linear activation function, suitable for regression tasks. The model utilizes the Adam optimizer alongside the mean squared error loss function. We partition the data into training and testing sets with a 70:30 ratio, reserving 20 % of the training data for validation. The ANN model undergoes training for 5000 epochs with a mini batch size = 70.

RF-based analysis: We here maintain the same 11 input features and 1 output feature as previously mentioned in the ANN. The training, testing, and validation sets remain consistent with those employed in the ANN-based analysis after outlier removal and normalization. Here we tune the hyperparameters [56,58] based on the performance of the validation set, and engage the same hyperparameters as fixed in the RF-based analysis of early mentioned complex mixtures except n_estimators = 3366, random_state = 42.

KNN-based analysis: Similar to the ANN and RF-based analyses mentioned above, we engage the preprocessed data, maintain the same

Table 4
Analyses from various ML models for training and testing on the 'urine and complex mixture' dataset.

Algorithm	MAE	MSE	RMSE	NRMSE	R^2	LOD (μM)	LOQ (μM)
ANN	0.076	0.013	0.117	0.341	**0.830**	1.206	4.020
RF	11.83	335.4	18.31	0.196	**0.929**	0.683	2.17
KNN	24.15	1157.9	34.02	0.363	**0.764**	1.335	4.452

Table 5
List of literature on the Electrochemical detection of CRT.

Sl. No	Material	Electrochemical Technique	Enzymatic/Non-enzymatic	Linear Range (µM)	LOD (µM)	Real Sample analyzed	Response Time	Ref
1	CNT-ABTS/ Nafion/	Amperometry	Non-enzymatic	0–21,300	11.0	Urine	<60 s	[60]
2	CuO/IL/ERGO	Amperometry	Non-enzymatic	10–2000	0.22	Human serum	5 s	[61]
3	PVC-NH_2	Potentiometry	Enzymatic	80–100,000	3	Human serum	10 s	[62]
4	Cu on /(SPCE).	CV/DPV	Non- enzymatic	6–378	0.074	Human blood	–	[31]
5	Fe–Cu–rGO	CV/DPV	Non - enzymatic	0.01–1000	0.01	Human blood	–	[63]
6	PANI/o-PD	potentiometry	Enzymatic	3160–39,000	3160	Fetal bovine serum	20 min	[64]
7	Calix[4]pyrrol	potentiometry	Non- enzymatic	1–10,000	0.63	Urine(100× dilution)	<20 s	[65]
8	Cu/Nafion	Amperometry	Non- enzymatic	2.2–132.6	0.68	Urine(100× dilution)	–	[23]
9	2- NBA	CV/DPV	Non- enzymatic	1000–25,000	500	Urine (2× dilution)	–	[66]
10	Cu NW/MSQD	Amperometry	Non- enzymatic	1.96–966.0	0.920	Urine (100×, 50× and 20×)	5 s	Current work

Abbreviations: Pvc: polyvinyl chloride; ERGO: electrochemically reduced GO; GNP: graphene nanoplatelet; PDA: polydopamine; SPCE: screen printed carbon electrodes; PANI: polyaniline; o-PD: *o*-phenylenediamine; NBA: nitrobenzaldehyde.

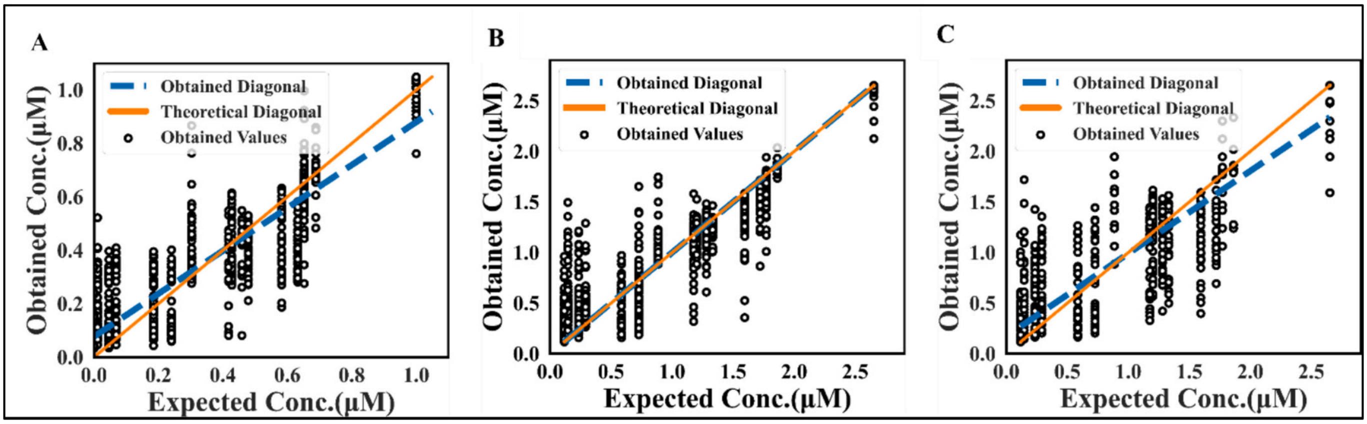

Fig. 6. Regression plots for training and testing on the 'urine and complex mixture' dataset. (A) ANN, (B) RF, and (C) KNN.

input/ output features, and keep similar training, testing, and validation sets. The hyperparameters [56,59] are fixed according to the KNN-based analysis of the aforementioned complex mixture.

We employed multiple performance metrics to evaluate the effectiveness of our models for CRT concentration prediction for on 'urine + complex mixture' dataset, as shown in Table 4. Here, we present the performances of ANN, RF, and KNN regressors with respect to MAE, MSE, RMSE, NRMSE, R^2, LOD, and LOQ. We obtained R^2 of 0.830, 0.929, and 0.764 from ANN, RF, and KNN, respectively. From this table, we can understand that RF performed the best, followed by ANN and KNN regressors.

In Fig. 6. (A), (B), and (C), we present the regression plots for predicting CRT concentration from urine and complex mixture data sets using ANN, RF, and KNN regressors, respectively.

4. Conclusions

In the present study, a targeted chemical interaction between CRT and CuNW/MSQD facilitates the electrochemical detection of CRT in a complex mixture solution containing interfering species, and urine samples. One of the major challenges in the development of selective electrochemical sensors lies in the deconvolution of complex and overlaid signals from interfering species. Hence, we combined data sets to accommodate larger variability and real-time scenarios by applying ML models on the electrochemical data set recorded using bare and CuNW/MSQD modified electrodes. The complexity of signals was addressed by training and testing different ML models and optimizing them using various feature matrices of electrochemical response. The high and low concentrations of interfering species were chosen to capture variability in the dataset and to account for differing reactivities of these species with the target analyte, CRT. This approach enables the mapping of reactivity across various concentration levels, reflecting their actual presence in biofluids. By including the effects of interfering species under realistic conditions, the dataset becomes more representative of practical scenarios. A larger variability factor was accommodated in the electrochemical data set to simulate the real-time scenarios where data will be coming from individuals with different metabolic profiles. We believe that by further miniaturization of such sensors into point-of-care testing devices combined with smart ML algorithms, CRT can directly be detected in complex biological matrices, in our case it is urine.

CRediT authorship contribution statement

Geethukrishnan: Writing – original draft, Writing – review & editing, Validation, Methodology, Investigation, Formal analysis, Conceptualization. **Paresh Prakash Bagde:** Writing – original draft, Visualization, Software, Methodology, Investigation, Formal analysis, Data curation, Conceptualization. **Sammishra KH:** Visualization, Methodology, Investigation, Formal analysis, Data curation. **Chandranath Adak:** Writing – review & editing, Validation, Methodology, Investigation, Formal analysis, Conceptualization, Supervision. **Rajendra P. Shukla:** Writing – review & editing, Writing – original draft, Software, Methodology, Formal analysis, Conceptualization, Supervision. **Kiran Kumar Tadi:** Writing – original draft, Writing – review & editing, Validation, Supervision, Project administration, Methodology, Investigation, Formal analysis, Data curation, Conceptualization.

Declaration of competing interest

The authors declare no conflict of interest.

Acknowledgments

Geethu Krishnan thanks the VIT, Chennai, for providing the PhD fellowship and grateful to Chemistry Departement, School of Advanced Sciences for facilitating the infracture and characterization facilities required for the research work.

Appendix A. Supplementary data

Supplementary data to this article can be found online at https://doi.org/10.1016/j.sbsr.2024.100727.

Data availability

No data was used for the research described in the article.

References

[1] D.-S. Ciou, P.-H. Wu, Y.-C. Huang, M.-C. Yang, S.-Y. Lee, C.-Y. Lin, Colorimetric and amperometric detection of urine creatinine based on the ABTS radical cation modified electrode, Sensors Actuators B Chem. 314 (2020) 128034, https://doi.org/10.1016/j.snb.2020.128034.

[2] S.N. Prabhu, S.C. Mukhopadhyay, C. Gooneratne, A.S. Davidson, G. Liu, Interdigital sensing system for detection of levels of creatinine from the samples, in: 2019 13th Int. Conf. Sens. Technol, 2019, pp. 1–6, https://doi.org/10.1109/ICST46873.2019.9047672.

[3] S.F. Sena, D. Syed, R.B. McComb, Effect of high creatine content on the Kodak single-slide method for creatinine, Clin. Chem. 34 (1988) 594–595, https://doi.org/10.1093/clinchem/34.3.594.

[4] Point-of-care creatinine testing in children at risk for sudden deterioration of renal function, Clin. Chem. Lab. Med. 45 (2007) 1536–1541, https://doi.org/10.1515/CCLM.2007.314.

[5] D. Lakshmi, B.B. Prasad, P.S. Sharma, Creatinine sensor based on a molecularly imprinted polymer-modified hanging mercury drop electrode, Talanta 70 (2006) 272–280, https://doi.org/10.1016/j.talanta.2006.02.038.

[6] A. Udy, S. O'Donoghue, V. D'Intini, H. Healy, J. Lipman, Point of care measurement of plasma creatinine in critically ill patients with acute kidney injury, Anaesthesia 64 (2009) 403–407, https://doi.org/10.1111/j.1365-2044.2008.05818.x.

[7] M. Jaffe, Ueber den Niederschlag, welchen Pikrinsäure in normalem Harn erzeugt und über eine neue Reaction des, Kreatinins 10 (1886) 391–400, https://doi.org/10.1515/bchm1.1886.10.5.391.

[8] S. Yadav, A. Kumar, C.S. Pundir, Amperometric creatinine biosensor based on covalently coimmobilized enzymes onto carboxylated multiwalled carbon nanotubes/polyaniline composite film, Anal. Biochem. 419 (2011) 277–283, https://doi.org/10.1016/j.ab.2011.07.032.

[9] S.C. Lo, K.S. Tsai, Glucose interference in Jaffe creatinine method: effect of calcium from peritoneal dialysate [3], Clin. Chem. 40 (1994) 2326–2327, https://doi.org/10.1093/clinchem/40.12.2326.

[10] C.J. Kochansky, T.G. Strein, Determination of uremic toxins in biofluids: creatinine, creatine, uric acid and xanthines, J. Chromatogr. B Biomed. Sci. Appl. 747 (2000) 217–227, https://doi.org/10.1016/S0378-4347(00)00119-5.

[11] P. Kumar, R. Jaiwal, C.S. Pundir, An improved amperometric creatinine biosensor based on nanoparticles of creatininase, creatinase and sarcosine oxidase, Anal. Biochem. 537 (2017) 41–49, https://doi.org/10.1016/j.ab.2017.08.022.

[12] C.S. Pundir, S. Yadav, A. Kumar, Creatinine sensors, TrAC - Trends Anal. Chem. 50 (2013) 42–52, https://doi.org/10.1016/j.trac.2013.04.013.

[13] M. Zhybak, V. Beni, M.Y. Vagin, E. Dempsey, A.P.F. Turner, Y. Korpan, Creatinine and urea biosensors based on a novel ammonium ion-selective copper-polyaniline nano-composite, Biosens. Bioelectron. 77 (2016) 505–511, https://doi.org/10.1016/j.bios.2015.10.009.

[14] T. Yasukawa, Y. Kiba, F. Mizutani, A dual electrochemical sensor based on a test-strip assay for the quantitative determination of albumin and creatinine, Anal. Sci. 31 (2015) 583–589, https://doi.org/10.2116/analsci.31.583.

[15] A.B. Monnappa, J.G. Manjunatha, A.S. Bhatt, Design of a Sensitive and Selective Voltammetric Sensor Based on a cationic surfactant-modified carbon paste electrode for the determination of Alloxan, ACS Omega 5 (2020) 23481–23490, https://doi.org/10.1021/acsomega.0c03517.

[16] X. Gao, R. Gui, H. Guo, Z. Wang, Q. Liu, Creatinine-induced specific signal responses and enzymeless ratiometric electrochemical detection based on copper nanoparticles electrodeposited on reduced graphene oxide-based hybrids, Sensors Actuators B Chem. 285 (2019) 201–208, https://doi.org/10.1016/j.snb.2019.01.057.

[17] D.A. Walsh, E. Dempsey, Comparison of electrochemical, electrophoretic and spectrophotometric methods for creatinine determination in biological fluids, Anal. Chim. Acta 459 (2002) 187–198, https://doi.org/10.1016/S0003-2670(02)00110-1.

[18] S. Tajik, H. Beitollahi, S.Z. Mohammadi, M. Azimzadeh, K. Zhang, Q. Van Le, Y. Yamauchi, H.W. Jang, M. Shokouhimehr, Recent developments in electrochemical sensors for detecting hydrazine with different modified electrodes, RSC Adv. 10 (2020) 30481–30498, https://doi.org/10.1039/D0RA03288C.

[19] H. Beitollahi, M. Shahsavari, I. Sheikhshoaie, S. Tajik, P.M. Jahani, S. Z. Mohammadi, A.A. Afshar, Amplified electrochemical sensor employing screen-printed electrode modified with Ni-ZIF-67 nanocomposite for high sensitive analysis of Sudan I in present bisphenol A, Food Chem. Toxicol. 161 (2022) 112824, https://doi.org/10.1016/j.fct.2022.112824.

[20] S. Tajik, A. Lohrasbi-Nejad, P. Mohammadzadeh Jahani, M.B. Askari, P. Salarizadeh, H. Beitollahi, Co-detection of carmoisine and tartrazine by carbon paste electrode modified with ionic liquid and MoO3/WO3 nanocomposite, J. Food Meas. Charact. 16 (2022) 722–730, https://doi.org/10.1007/s11694-021-01201-4.

[21] S.Z. Mohammadi, H. Beitollahi, E. Bani Asadi, Electrochemical determination of hydrazine using a ZrO2 nanoparticles-modified carbon paste electrode, Environ. Monit. Assess. 187 (2015) 122, https://doi.org/10.1007/s10661-015-4309-9.

[22] N. Hareesha, J.G. Manjunatha, Z.A. Alothman, M. Sillanpää, Simple and affordable graphene nano-platelets and carbon nanocomposite surface decorated with cetrimonium bromide as a highly responsive electrochemical sensor for rutin detection, J. Electroanal. Chem. 917 (2022) 116388, https://doi.org/10.1016/j.jelechem.2022.116388.

[23] C.-H. Chen, M.S. Lin, A novel structural specific creatinine sensing scheme for the determination of the urine creatinine, Biosens. Bioelectron. 31 (2012) 90–94, https://doi.org/10.1016/j.bios.2011.09.043.

[24] V. Kumar, S. Hebbar, R. Kalam, S. Panwar, S. Prasad, S.S. Srikanta, P. R. Krishnaswamy, N. Bhat, Creatinine-iron complex and its use in electrochemical measurement of urine creatinine, IEEE Sensors J. 18 (2017) 830–836.

[25] K.B. Viswanath, R. Devasenathipathy, S.F. Wang, V.S. Vasantha, A new route for the Enzymeless trace level detection of creatinine based on reduced graphene oxide/silver nanocomposite biosensor, Electroanalysis 29 (2017) 559–565, https://doi.org/10.1002/elan.201600425.

[26] R.K. Rakesh Kumar, M.O. Shaikh, C.-H. Chuang, A review of recent advances in non-enzymatic electrochemical creatinine biosensing, Anal. Chim. Acta 1183 (2021) 338748, https://doi.org/10.1016/j.aca.2021.338748.

[27] R. Vaishya, S. Arora, B. Singh, V. Mallika, S. Arora, Modification of Jaffe's kinetic method decreases bilirubin interference: a preliminary report, Indian J. Clin. Biochem. 25 (2010) 64–66, https://doi.org/10.1007/s12291-010-0013-2.

[28] Y. Wang, S. Wang, L. Tao, Q. Min, J. Xiang, Q. Wang, J. Xie, Y. Yue, S. Wu, X. Li, H. Ding, A disposable electrochemical sensor for simultaneous determination of norepinephrine and serotonin in rat cerebrospinal fluid based on MWNTs-ZnO/chitosan composites modified screen-printed electrode, Biosens. Bioelectron. 65 (2015) 31–38, https://doi.org/10.1016/j.bios.2014.09.099.

[29] H. Jin, B. Baek, D. Kim, F. Wu, J.D. Batteas, J. Cheon, D.H. Son, Effects of direct solvent-quantum dot interaction on the optical properties of colloidal monolayer WS2 quantum dots, Nano Lett. 17 (2017) 7471–7477, https://doi.org/10.1021/acs.nanolett.7b03381.

[30] M. Mitewa, Coordination properties of the bioligands creatinine and creatine in various reaction media, Coord. Chem. Rev. 140 (1995) 1–25.

[31] J. Raveendran, P.E. Resmi, T. Ramachandran, B.G. Nair, T.G. Satheesh Babu, Fabrication of a disposable non-enzymatic electrochemical creatinine sensor, sensors actuators, B Chem. 243 (2017) 589–595, https://doi.org/10.1016/j.snb.2016.11.158.

[32] S. Reddy, B.E.K. Swamy, H. Jayadevappa, CuO nanoparticle sensor for the electrochemical determination of dopamine, Electrochim. Acta 61 (2012) 78–86.

[33] M.M. Charithra, J.G. Manjunatha, Electrochemical sensing of adrenaline using surface modified carbon nanotube paste electrode, Mater. Chem. Phys. 262 (2021) 124293, https://doi.org/10.1016/j.matchemphys.2021.124293.

[34] G. Tigari, J.G. Manjunatha, Poly(glutamine) film-coated carbon nanotube paste electrode for the determination of curcumin with vanillin: an electroanalytical approach, Monatshefte Für Chemie - Chem. Mon. 151 (2020) 1681–1688, https://doi.org/10.1007/s00706-020-02700-8.

[35] M. Manjunatha Charithra, J.G. Manjunatha, Electrochemical sensing of paracetamol using Electropolymerised and sodium lauryl sulfate modified carbon nanotube paste electrode, ChemistrySelect 5 (2020) 9323–9329, https://doi.org/10.1002/slct.202002626.

[36] S.R. Darmakkolla, H. Tran, A. Gupta, S.B. Rananavare, A method to derivatize surface silanol groups to Si-alkyl groups in carbon-doped silicon oxides, RSC Adv. 6 (2016) 93219–93230.

[37] S. Ye, A.R. Rathmell, I.E. Stewart, Y.-C. Ha, A.R. Wilson, Z. Chen, B.J. Wiley, A rapid synthesis of high aspect ratio copper nanowires for high-performance transparent conducting films, Chem. Commun. 50 (2014) 2562–2564.

[38] S.P. Figerez, K.K. Tadi, K.R. Sahoo, R. Sharma, R.K. Biroju, A. Gigi, K.A. Anand, G. Kalita, T.N. Narayanan, Molybdenum disulfide–graphene van der Waals heterostructures as stable and sensitive electrochemical sensing platforms, Tungsten 2 (2020) 411–422.

[39] J. Kabel, S. Sharma, A. Acharya, D. Zhang, Y.K. Yap, Molybdenum disulfide quantum dots: properties, synthesis, and applications, C 7 (2021) 45.

[40] S.R. Darmakkolla, M. Ghobadi, L. Lampert, A.F. Pareira, A. Jenike, M. Tahir, S. B. Rananavare, Morphology-controlled copper nanowire synthesis and magnetic field assisted self-assembly, Nanoscale 11 (2019) 2679–2686, https://doi.org/10.1039/c8nr06876c.

[41] S. Pal, K.K. Tadi, P.M. Sudeep, S. Radhakrishnan, T.N. Narayanan, Temperature assisted shear exfoliation of layered crystals for the large-scale synthesis of

catalytically active luminescent quantum dots, Mater. Chem. Front. 1 (2017) 319–325, https://doi.org/10.1039/c6qm00081a.

[42] H. Harsojo, L. Puspita, D. Mardiansyah, R. Roto, K. Triyana, The roles of hydrazine and ethylene diamine in wet synthesis of cu Nano wire, Indones. J. Chem. 17 (2017) 43, https://doi.org/10.22146/ijc.23618.

[43] S. Xu, D. Li, P. Wu, One-pot, facile, and versatile synthesis of monolayer MoS2/WS2 quantum dots as bioimaging probes and efficient electrocatalysts for hydrogen evolution reaction, Adv. Funct. Mater. 25 (2015) 1127–1136.

[44] L. Ali, F. Subhan, M. Ayaz, S.S. Ul Hassan, C.C. Byeon, J.S. Kim, S. Bungau, Exfoliation of MoS2 quantum dots: recent Progress and challenges, Nanomaterials 12 (2022) 3465.

[45] L. Ali, S. Bang, Y.J. Lee, C.C. Byeon, Ion-intercalation assisted Solvothermal synthesis and optical characterization of MoS 2 quantum dots, J. Korean Phys. Soc. 74 (2019) 191–195.

[46] X.L. Wu, J.Y. Fan, T. Qiu, X. Yang, G.G. Siu, P.K. Chu, Experimental evidence for the quantum confinement effect in 3 C-SiC nanocrystallites, Phys. Rev. Lett. 94 (2005) 26102.

[47] V. Štengl, J. Henych, Strongly luminescent monolayered MoS 2 prepared by effective ultrasound exfoliation, Nanoscale 5 (2013) 3387–3394.

[48] V.K. Singh, H. Mishra, R. Ali, S. Umrao, R. Srivastava, S. Abraham, A. Misra, V. N. Singh, H. Mishra, R.S. Tiwari, In situ functionalized fluorescent WS2-QDs as sensitive and selective probe for Fe3+ and a detailed study of its fluorescence quenching, ACS Appl. Nano Mater. 2 (2018) 566–576.

[49] A. Molina-Sanchez, L. Wirtz, Phonons in single-layer and few-layer MoS 2 and WS 2, Phys. Rev. B 84 (2011) 155413.

[50] J.F. Xu, W. Ji, Z.X. Shen, W.S. Li, S.H. Tang, X.R. Ye, D.Z. Jia, X.Q. Xin, Raman spectra of CuO nanocrystals, J. Raman Spectrosc. 30 (1999) 413–415.

[51] K. Ngamchuea, S. Wannapaiboon, P. Nongkhunsan, P. Hirunsit, I. Fongkaew, Structural and electrochemical analysis of copper-creatinine complexes: application in creatinine detection, J. Electrochem. Soc. 169 (2022) 20567, https://doi.org/10.1149/1945-7111/ac5346.

[52] R.K. Biroju, D. Das, R. Sharma, S. Pal, L.P.L. Mawlong, K. Bhorkar, P.K. Giri, A. K. Singh, T.N. Narayanan, Hydrogen evolution reaction activity of graphene–MoS2 van der Waals heterostructures, ACS Energy Lett. 2 (2017) 1355–1361.

[53] R.P. Shukla, H. Ben-Yoav, A chitosan-carbon nanotube-modified microelectrode for in situ detection of blood levels of the antipsychotic clozapine in a finger-pricked sample volume, Adv. Healthc. Mater. 8 (2019) e1900462, https://doi.org/10.1002/adhm.201900462.

[54] S. Haykin, Neural Networks: A Comprehensive Foundation, 1st ed., Prentice Hall PTR, USA, 1994.

[55] M. Fratello, R. Tagliaferri, Decision Trees and Random Forests, 2018, https://doi.org/10.1016/B978-0-12-809633-8.20337-3.

[56] D. Larose, C. Larose, k-Nearest Neighbor Algorithm, 2014, pp. 149–164, https://doi.org/10.1002/9781118874059.ch7.

[57] M. Hubert, S. Van der Veeken, Outlier detection for skewed data, J. Chemom. 22 (2008) 235–246, https://doi.org/10.1002/cem.1123.

[58] D. Singh, B. Singh, Feature wise normalization: an effective way of normalizing data, Pattern Recogn. 122 (2021) 108307, https://doi.org/10.1016/j.patcog.2021.108307.

[59] F. Pedregosa, G. Varoquaux, A. Gramfort, V. Michel, B. Thirion, O. Grisel, M. Blondel, P. Prettenhofer, R. Weiss, V. Dubourg, J. Vanderplas, A. Passos, D. Cournapeau, M. Brucher, M. Perrot, E. Duchesnay, G. Louppe, Scikit-learn: machine learning in Python, J. Mach. Learn. Res. 12 (2012).

[60] C.L. Gonzalez-Gallardo, N. Arjona, L. Álvarez-Contreras, M. Guerra-Balcázar, Electrochemical creatinine detection for advanced point-of-care sensing devices: a review, RSC Adv. 12 (2022) 30785–30802, https://doi.org/10.1039/d2ra04479j.

[61] S. Boobphahom, N. Ruecha, N. Rodthongkum, O. Chailapakul, V.T. Remcho, A copper oxide-ionic liquid/reduced graphene oxide composite sensor enabled by digital dispensing: non-enzymatic paper-based microfluidic determination of creatinine in human blood serum, Anal. Chim. Acta 1083 (2019) 110–118, https://doi.org/10.1016/j.aca.2019.07.029.

[62] J.-S. Do, Y.-H. Chang, Optimizing the sensing performance of amperometric creatinine detection based on creatinine deiminase/Nafion®-nanostructured polyaniline composite film by mixture design method, Sensors and Actuators Reports. 5 (2023) 100135, https://doi.org/10.1016/j.snr.2022.100135.

[63] P. Singh, S. Mandal, D. Roy, N. Chanda, Facile detection of blood creatinine using binary copper-iron oxide and rGO-based nanocomposite on 3D printed ag-electrode under poc settings, ACS Biomater Sci. Eng. 7 (2021) 3446–3458, https://doi.org/10.1021/acsbiomaterials.1c00484.

[64] C.-J. Huang, J.-L. Lin, P.-H. Chen, M.-J. Syu, G.-B. Lee, A multi-functional electrochemical sensing system using microfluidic technology for the detection of urea and creatinine, Electrophoresis 32 (2011) 931–938, https://doi.org/10.1002/elps.201000679.

[65] T. Guinovart, D. Hernández-Alonso, L. Adriaenssens, P. Blondeau, F.X. Rius, P. Ballester, F.J. Andrade, Characterization of a new ionophore-based ion-selective electrode for the potentiometric determination of creatinine in urine, Biosens. Bioelectron. 87 (2017) 587–592, https://doi.org/10.1016/j.bios.2016.08.025.

[66] N. Hussain, P. Puzari, A novel method for electrochemical determination of creatinine in human urine based on its reaction with 2-nitrobenzaldehyde using a glassy carbon electrode, J. Appl. Electrochem. (2023), https://doi.org/10.1007/s10800-023-01938-4.